Supporting Information for

Crustal earthquakes in the Cook Inlet and Susitna region of southern Alaska

Vipul Silwal, Carl Tape, and Anthony Lomax

Tectonophysics

June 12, 2018

Contents

S1 Misfit reward factors

This section supports Section 3.3.

As summarized in Section 7.3 of *Silwal and Tape* (2016), while fitting observed and synthetic waveforms, we frequently encounter cases where the total normalized misfit when using more data (larger time-windows, wider bandpass, and more stations) is larger than the one obtained when using fewer data. In essence, overfitting can occur when using fewer waveforms: the synthetic waveforms may result in a low misfit, yet the moment tensor solution may be incorrect.

This happens because it is much easier to fit a single waveform (or waveforms for fewer stations) and could result in a lower misfit for a wrong solution (Figure S2). We address this by modifying our misfit function to include scale factors that reward the use of:

1. a longer time window for Pnl and surface waves
2. a broader bandpass for Pnl and surface waves
3. more stations

This weighting has been used for full moment tensor inversions in *Alvizuri et al.* (2018) and *Alvizuri and Tape* (2018).

S1.1 Waveform reward factor for using longer time windows and a broader bandpass

For each station j and each time window i, we consider a weighting matrix in Equation (1). Our choice is a constant-valued diagonal matrix

$$\mathbf{W}_{ij} = \frac{w_{ij}}{d_{ij} b_{ij}} \mathbf{I} \tag{S1}$$

where w_{ij} is the user-specified weight for the ijth time window, d_{ij} is the length of window in seconds, and b_{ij} is the length of bandpass in Hertz. In our study, $w_{ij} = 1$ always, but there may be reason to test weighting body waves and surface waves differently (*Alvizuri and Tape*, 2016) or to emphasize or demphasize a particular time window. The longer time windows and wider bandpass will lead to smaller values of the diagonal of $\mathbf{W}_{ij}$, resulting in lower misfit values (Eq. 1) and larger VR values.

S1.2 Station reward factor for using more stations

The final scaled misfit function (Eq. 3)

$$\Phi(M, N_s) = h(N_s) \times \Phi(M), \tag{S2}$$

is scaled by a weighting function $h(N_s)$ so that the total misfit $\Phi(M)$ is rewarded for using more stations. We define this weighting function as

$$h(N_s) = 0.5 + 1.5\, e^{-N_s/C} \tag{S3}$$

where N_s is the number of stations and C represents a reference number of stations and governs the shape of the weighting function (see Figure S1). When $N_s = C$, $h(N_s) = 0.5 + 1.5\, e^{-1} \approx 1$. As N_s increases, $h(N_s)$ decreases, leading to a lower misfit function (i.e., reward). As N_s decreases, $h(N_s)$ increases, leading to a higher misfit function (i.e., penalty). The constant 0.5 is included to prevent the misfit from going to zero for the cases where large number of stations are used.

We show an example of the impact of Equation (S3) for an example event. With $N_s = 3$ and $C = 7$, we have $h(N_s) \approx 1.5$, which increases the misfit function and leads to a very low VR value, in spite of the appearance of well-fitting waveforms (Figure S2a). With $N_s = 5$, we have a different $h(N_s)$ and also a different best-fitting moment tensor (Figure S2b). Our preferred solution uses $N_s = 9$ and is shown in Figure S3. Figure S4 demonstrates that using more stations will not always results in lower misfit (and higher VR). Here we had a 10th station that is a clear outlier. Thanks to the use of an L1-norm in the misfit function, we are able to still obtain the same best-fitting moment tensor (Figure S3), but the VR value is now muc lower (26.2 vs 51.8), despite having a lower penalty factor for using more stations. If the 10th station had comparable or better waveform fits than the other stations, then we would expect the lower penalty factor to result in lower misfit and higher VR.

References

Alvizuri, C., and C. Tape (2016), Full moment tensors for small events ($M_{\mathrm{w}} < 3$) at Uturuncu volcano, Bolivia, *Geophys. J. Int.*, *206*, 1761–1783, doi:10.1093/gji/ggw247.

Alvizuri, C., and C. Tape (2018), Full moment tensor analysis of nuclear explosions in North Korea, *Seismol. Res. Lett.* (submitted).

Alvizuri, C., V. Silwal, L. Krischer, and C. Tape (2018), Estimation of full moment tensors, including uncertainties, for nuclear explosions, volcanic events, and earthquakes, *J. Geophys. Res. Solid Earth* (in press), doi:10.1029/2017JB015325.

Brockman, S. R., A. F. Espinosa, and J. A. Michael (1988), *Catalog of Intensities and Magnitudes for Earthquakes in Alaska and the Aleutian Islands—1786–1981*, U.S. Geol. Survey Bulletin 1840.

Doser, D. I., and W. A. Brown (2001), A study of historic earthquakes of the Prince William Sound, Alaska, Region, *Bull. Seismol. Soc. Am.*, *91*(4), 842–857.

Engdahl, E. R., and A. Villasenor (2002), Global seismicity: 1900–1999, in *International Handbook of Earthquake and Engineering Seismology*, *International Geophysics Series*, vol. 81A, edited by W. H. K. Lee, H. Kanamori, P. C. Jennings, and C. Kisslinger, pp. 665–690, Academic Press, London.

Gutenberg, B., and C. F. Richter (1954), *Seismicity of the Earth and Associated Phenomena*, 2 ed., Princeton U. Press, Princeton, New Jersey, USA.

Kirschner, C. E. (1988), Map Showing Sedimentary Basins of Onshore and Continental Shelf Areas, Alaska, U.S. Geol. Survey Miscellaneous Investigation Series I-1873.

Li, J., G. A. Abers, Y. Kim, and D. Christensen (2013), Alaska megathrust 1: Seismicity 43 years after the great 1964 Alaska megathrust earthquake, *J. Geophys. Res.*, *118*, 4861–4871, doi:10.1002/jgrb.50358.

Lomax, A., J. Virieux, P. Volant, and C. Berge (2000), Probabilistic earthquake location in 3D and layered models: Introduction of a Metropolis-Gibbs method and comparison with linear locations, in *Advances in Seismic Event Location*, edited by C. H. Thurber and N. Rabinowitz, pp. 101–134, Kluwer, Amsterdam.

Lomax, A., V. Silwal, and C. Tape (2018), Hypocenter estimation for 14 earthquakes in south-central Alaska (1929–1975), ScholarWorks@UA at `http://hdl.handle.net/11122/8380`: descriptor file and zipped set of text files for each earthquake.

Silwal, V., and C. Tape (2016), Seismic moment tensors and estimated uncertainties in southern Alaska, *J. Geophys. Res. Solid Earth*, *121*, 2772–2797, doi:10.1002/2015JB012588.

Storchak, D. A., D. Di Giacomo, I. Bondár, E. R. Engdahl, J. Harris, W. H. K. Lee, A. Villaseñor, and P. Bormann (2013), Public release of the ISC–GEM Global Instrumental Earthquake Catalogue (1900–2009), *Seismol. Res. Lett.*, *84*(5), 810–815, doi:10.1785/0220130034.

Table S1: Source location and origin time for 1933, 1943 and 1954 earthquakes from various sources. See Figures 6 and 12 for locations on a map.

label	origin time	lat	lon	depth	reference
L33	1933-04-27 02:36:07.115	61.00	-151.07	0	this study
I33	1933-04-27 02:36:07.770	61.10	-151.06	15 ± 4	*Storchak et al.* (2013)
G33	1933-04-27 02:36:04	61.25	-150.75	0	*Gutenberg and Richter* (1954)
E33	1933-04-27 02:36:11.510	60.99	-151.00	35	*Engdahl and Villasenor* (2002)
D33	1933-04-27 02:36	61.11	-150.85	9 ± 4	*Doser and Brown* (2001)
L43	1943-11-03 14:32:22.982	61.66	-151.00	17	This study
I43	1943-11-03 14:32:20.840	61.79	-151.00	15 ± 9	*Storchak et al.* (2013)
G43	1943-11-03 14:32:17	61.75	-151.00	0	*Gutenberg and Richter* (1954)
E43	1943-11-03 14:32:24.120	61.63	-151.00	35	*Engdahl and Villasenor* (2002)
D43	1943-11-03 14:32	61.74	-150.80	27 ± 4	*Doser and Brown* (2001)
L54	1954-10-03 11:18:49.136	60.52	-150.51	56	This study
I54	1954-10-03 11:18:48.530	60.65	-150.39	62 ± 5	*Storchak et al.* (2013)
E54	1954-10-03 11:18:47	60.70	-150.30	64	*Engdahl and Villasenor* (2002)
D54	1954-10-03 11:18	60.68	-150.45	60 ± 10	*Doser and Brown* (2001)

Table S2: Double couple moment tensor solutions for 9 crustal earthquakes in the Beluga region (Table 1).

label	eid	lat	lon	strike	dip	rake	M_{w}	depth	Nstn
1	2008-01-26 04:29:42	61.56	-151.23	141	50	67	3.0	11.0	19
2	2008-02-05 03:51:42	61.55	-151.28	46	54	58	2.6	2.0	14
3	2009-05-16 01:51:04	61.66	-151.25	61	49	68	2.9	7.0	10
4	2010-03-28 16:05:36	61.69	-151.34	326	70	-29	3.0	5.0	6
5	2012-03-06 06:12:58	61.54	-151.25	63	84	9	2.6	12.0	12
6	2012-06-29 11:07:39	61.62	-151.30	168	38	85	2.5	8.0	7
7	2014-01-24 12:07:03	61.65	-151.26	342	50	-33	3.0	8.0	9
8	2014-07-14 06:04:10	61.59	-151.29	165	37	70	3.0	11.0	14
9	2016-04-18 18:02:12	61.61	-151.22	8	44	82	2.6	7.0	10

Table S3: Double couple moment tensor solutions for 22 crustal earthquakes in the Upper Cook Inlet region (Table 1).

label	origin time	latitude	longitude	strike	dip	rake	M_w	depth	stations
1	2008-04-08 17:16:30	61.06	-150.85	229	48	71	2.6	16.0	32
2	2008-04-15 08:42:17	60.97	-151.13	135	41	70	2.8	13.0	30
3	2008-10-06 18:24:38	61.15	-150.76	147	60	38	2.6	13.0	16
4	2008-11-22 05:30:47	60.99	-151.16	156	54	72	2.9	10.0	15
5	2009-05-02 09:50:52	60.88	-150.93	152	46	33	2.6	5.0	16
6	2009-09-05 01:52:36	60.94	-151.08	6	65	90	2.9	15.0	9
7	2010-06-18 08:10:34	61.09	-151.10	49	58	58	2.6	7.0	6
8	2010-10-13 14:45:37	61.08	-150.94	14	83	35	2.8	11.0	11
9	2010-12-28 23:08:30	61.00	-150.94	21	34	60	2.8	13.0	7
10	2012-02-13 17:40:33	60.93	-151.09	311	42	29	2.5	10.0	8
11	2012-03-08 10:57:43	61.01	-150.91	154	44	54	4.0	10.0	11
12	2012-08-02 06:11:38	60.82	-151.02	208	31	84	2.9	18.0	12
13	2013-03-24 15:24:30	60.92	-150.83	348	40	46	2.7	12.0	12
14	2013-03-26 04:30:06	60.93	-150.86	253	62	-81	2.9	10.0	13
15	2014-02-03 00:03:07	60.92	-151.13	11	32	79	2.9	15.0	17
16	2014-11-15 03:01:00	60.76	-151.07	214	58	85	2.5	20.0	23
17	2014-12-11 00:48:39	60.74	-151.03	33	35	-70	3.0	20.0	22
18	2014-12-28 17:00:32	60.95	-150.87	320	16	58	3.1	20.0	23
19	2015-03-15 08:56:11	61.03	-150.79	284	34	50	2.5	15.0	21
20	2015-07-27 02:21:54	60.98	-150.94	319	50	24	3.5	16.0	42
21	2015-08-30 21:27:12	61.00	-150.96	151	37	48	2.6	15.0	31
22	2015-11-24 21:25:57	60.94	-150.82	152	53	35	2.7	20.0	32

Table S4: Double couple moment tensor solutions for 22 crustal earthquakes in the Susitna region (Table 1).

label	eid	lat	lon	strike	dip	rake	M_w	depth	Nstn
1	2007-12-19 21:58:56	62.23	-150.13	166	58	62	3.2	8.0	16
2	2008-04-18 04:14:58	62.05	-150.50	331	8	-81	3.2	3.0	10
3	2008-06-02 17:27:40	61.88	-150.10	172	37	65	3.6	6.0	23
4	2010-07-08 03:15:49	61.81	-150.50	41	30	77	4.8	15.0	9
5	2010-12-01 23:19:44	62.30	-150.11	355	59	61	3.2	10.0	9
6	2010-12-14 02:22:37	62.28	-150.27	3	24	73	3.6	21.0	8
7	2011-04-05 18:30:24	62.31	-150.03	24	54	68	3.4	12.0	9
8	2011-04-16 06:01:41	62.31	-149.99	24	54	68	3.1	11.0	12
9	2011-10-21 17:09:40	61.90	-150.25	162	47	66	3.7	3.0	12
10	2011-12-03 09:33:58	61.97	-150.93	17	82	88	4.1	6.0	17
11	2012-01-27 17:10:28	61.80	-150.18	327	54	76	3.1	10.0	15
12	2012-04-29 10:57:57	62.07	-149.99	131	42	67	3.2	6.0	16
13	2013-01-20 21:56:58	62.19	-150.40	12	31	86	3.4	15.0	12
14	2013-09-23 09:21:18	61.63	-150.65	186	42	74	3.7	6.0	17
15	2013-09-30 06:32:02	61.92	-150.90	163	48	84	3.2	10.0	17
16	2014-01-21 14:29:20	62.09	-150.37	192	38	72	3.1	16.0	17
17	2015-01-19 10:36:11	62.19	-150.57	25	50	76	4.0	10.0	23
18	2015-05-18 15:49:10	61.94	-150.45	6	40	89	4.2	21.0	17
19	2016-01-18 04:05:56	62.10	-150.64	156	80	39	4.5	10.0	28
20	2016-05-29 23:49:37	61.87	-150.28	168	71	30	3.1	16.0	24
21	2016-12-01 23:55:55	61.86	-150.27	354	53	31	3.0	18.0	27
22	2016-12-04 13:15:44	61.97	-150.90	117	42	38	4.2	8.0	27

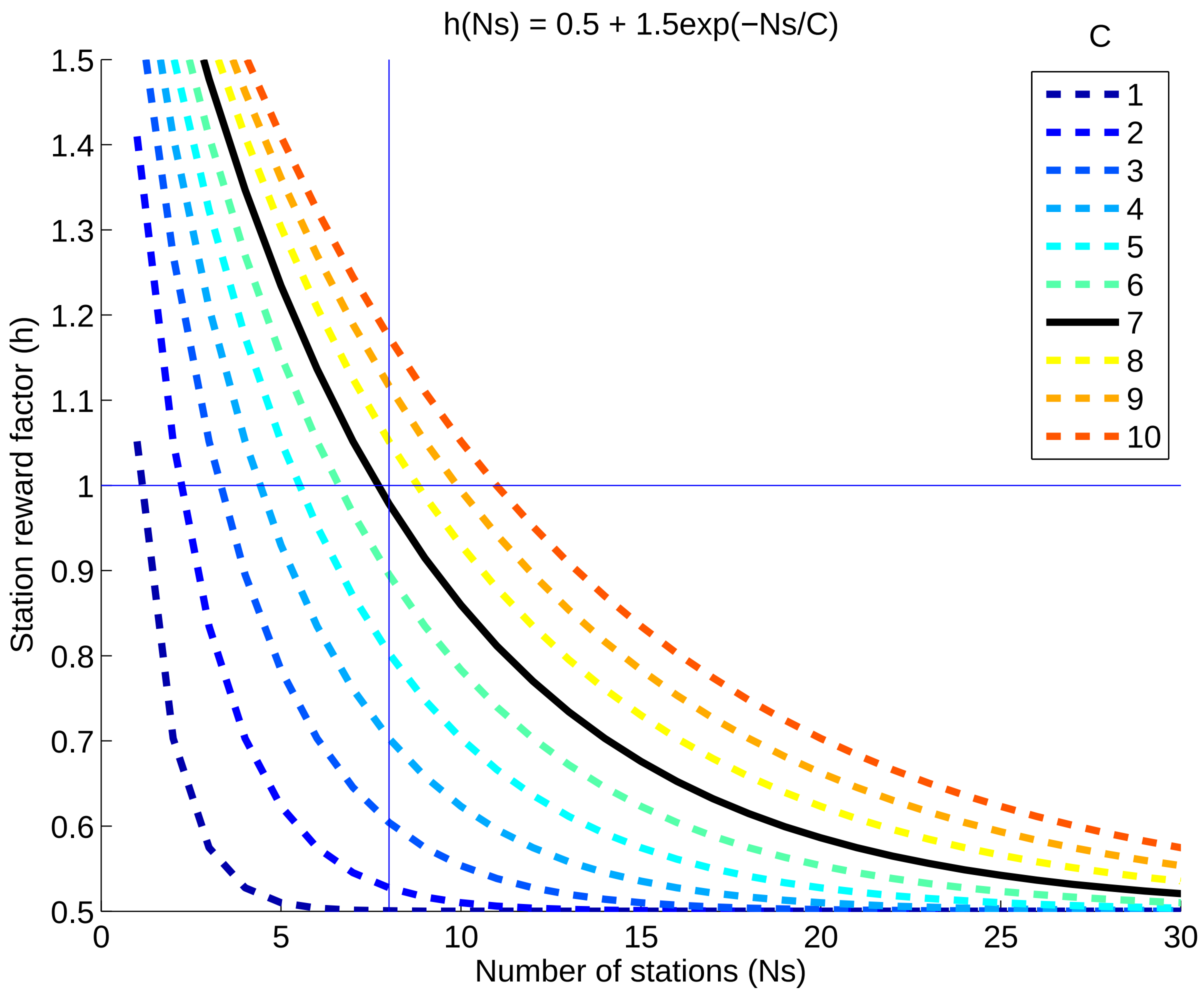

Figure S1: Plotting the station reward factor $h(N_s)$ (Eq. S3), which is used in the misfit function (Eq. 3). Our chosen function is for $C = 7$ (thick black line). The function $h(N_s)$ is approximately the same for $N_s = C$, and it will increase (penalty) for fewer stations and decrease (reward) for more stations.

(a)

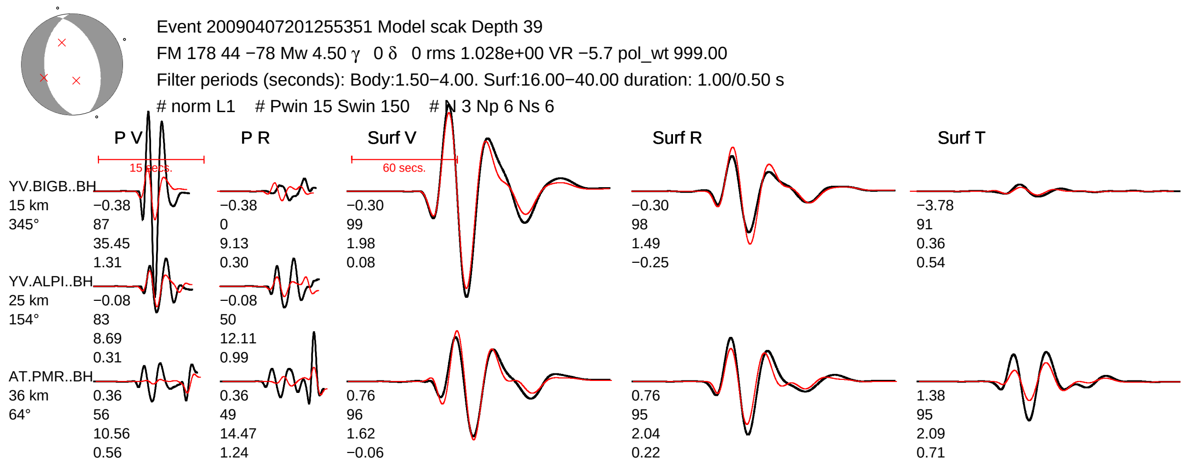

(b)

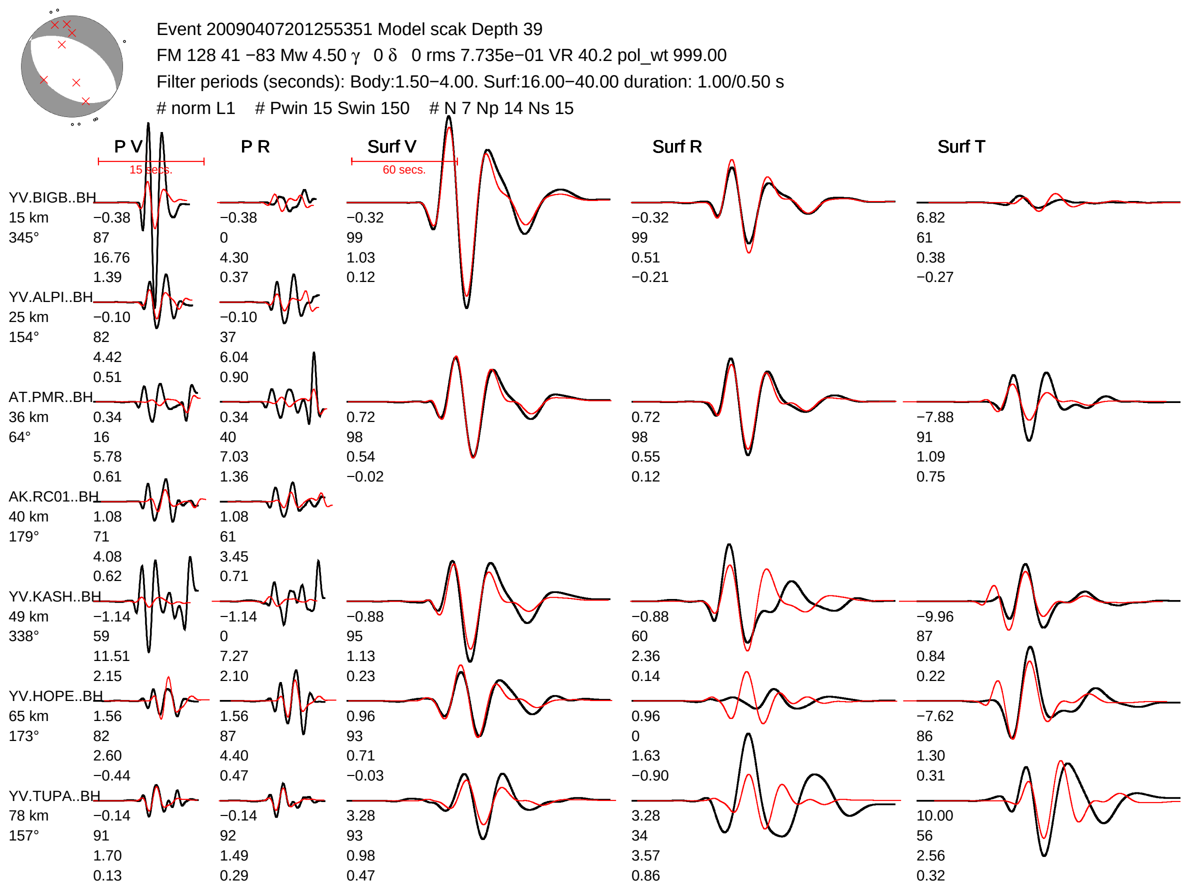

Figure S2: The effect of the number of stations on moment tensor solutions. Best-fitting moment tensor and waveform fits when using (a) 3 stations and (b) 7 stations. Notice the increase in *VR* (and the decrease in the RMS misfit) as we increase the number of stations; this is due to the station reward factor (Eq. S3). Also compare the beachballs with the preferred solution in Figure S3.

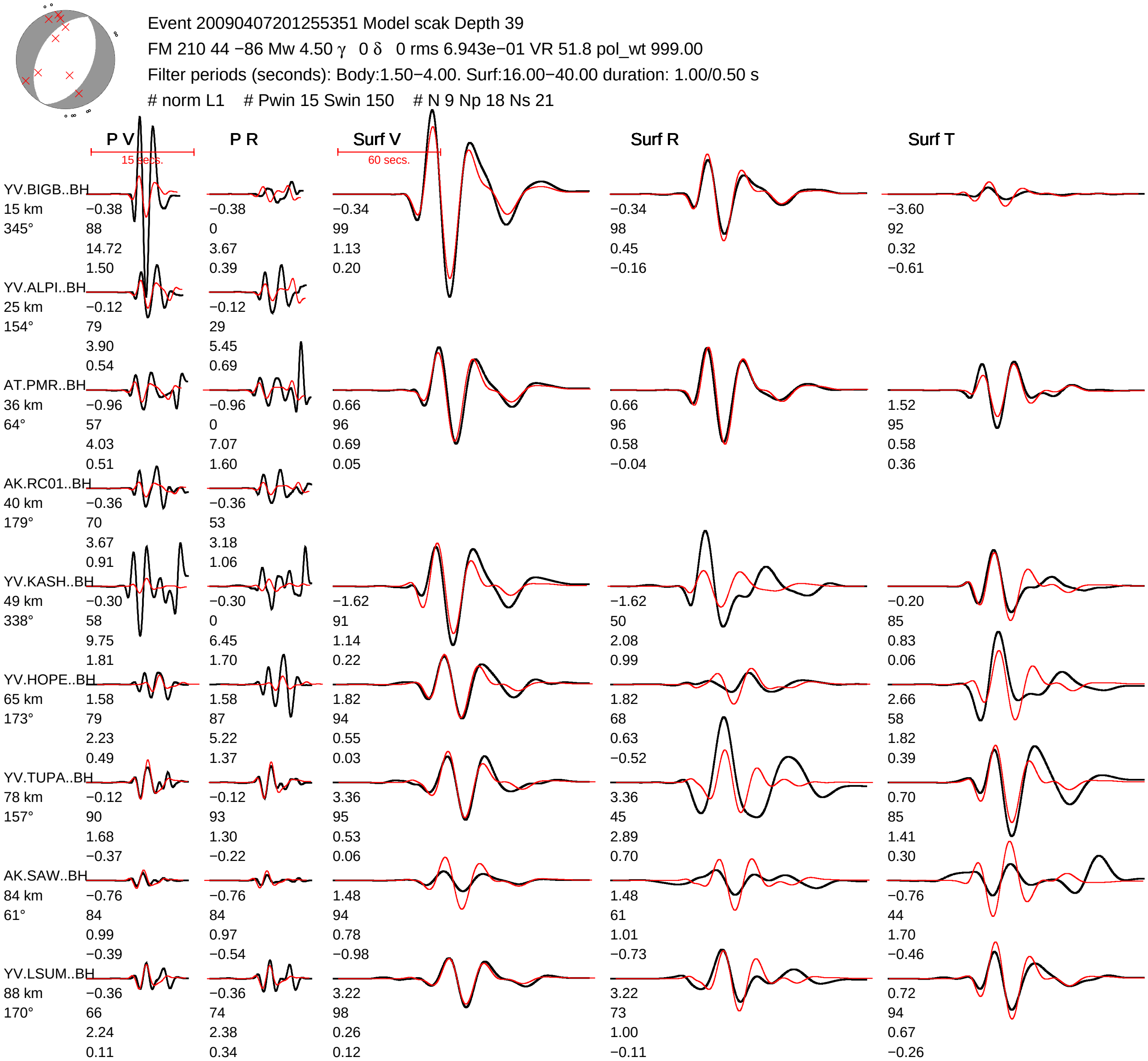

Figure S3: Waveform fits when using 9 stations instead of fewer stations (Figure S2). Here the *VR* is higher due to the station reward factor (Eq. S3).

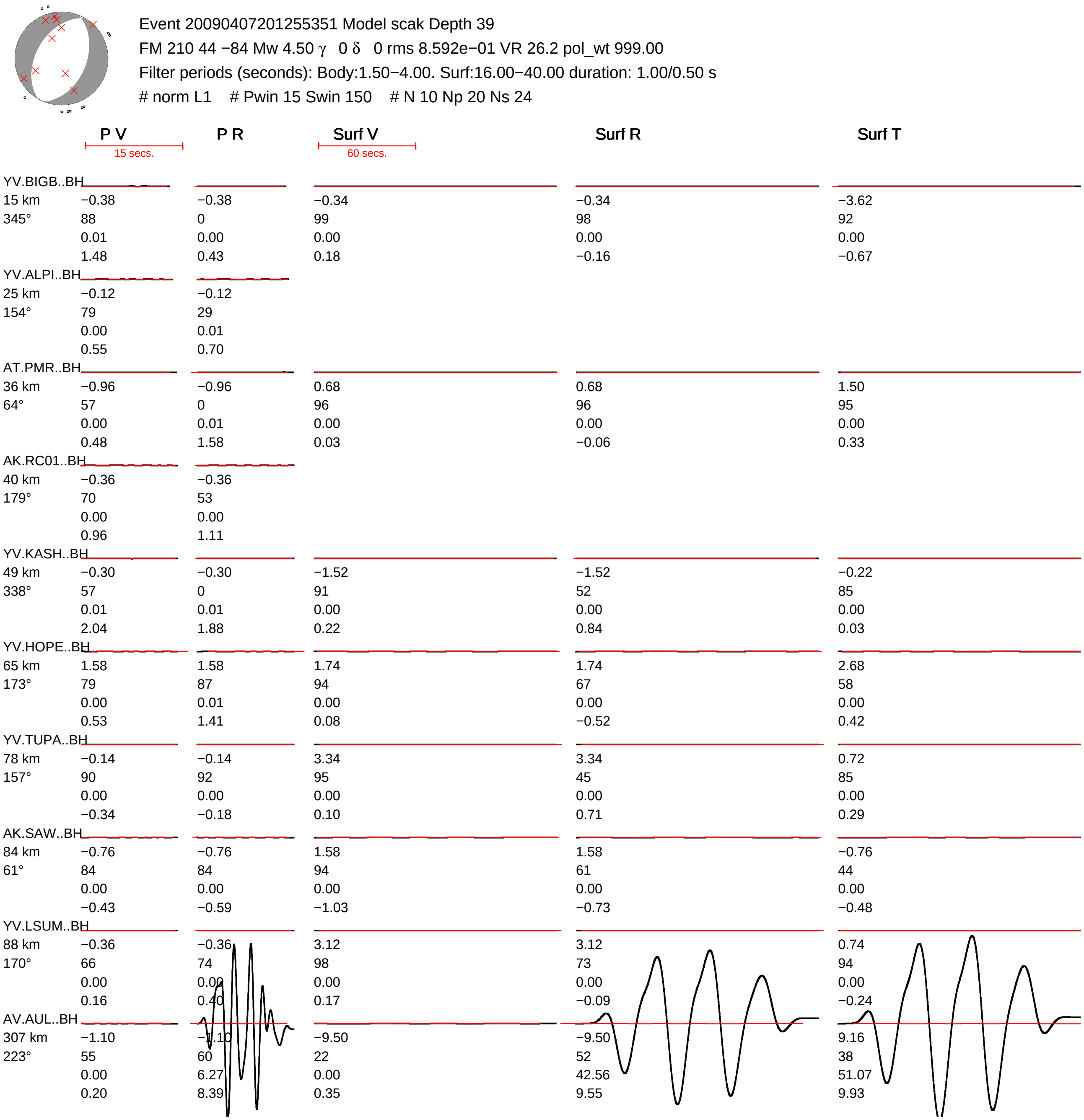

Figure S4: Waveform fits when using 10 stations. There are more stations than in Figure S3, which will lead to a lower value of $h(N_s)$ (greater reward). However, waveforms from the newly added station, AV.AUL, are clearly bad, which results in a VR that is lower than in Figure S3, despite having more stations. The anomalous amplitude of AV.AUL causes the other waveforms not to be visible on this plotting scale; however, they are expected to be very similar to those in Figure S3. Note that the best-fitting moment tensor is similar to what is obtained in Figure S3; this is due to the use of an L1 misfit function that is insensitive to outliers.

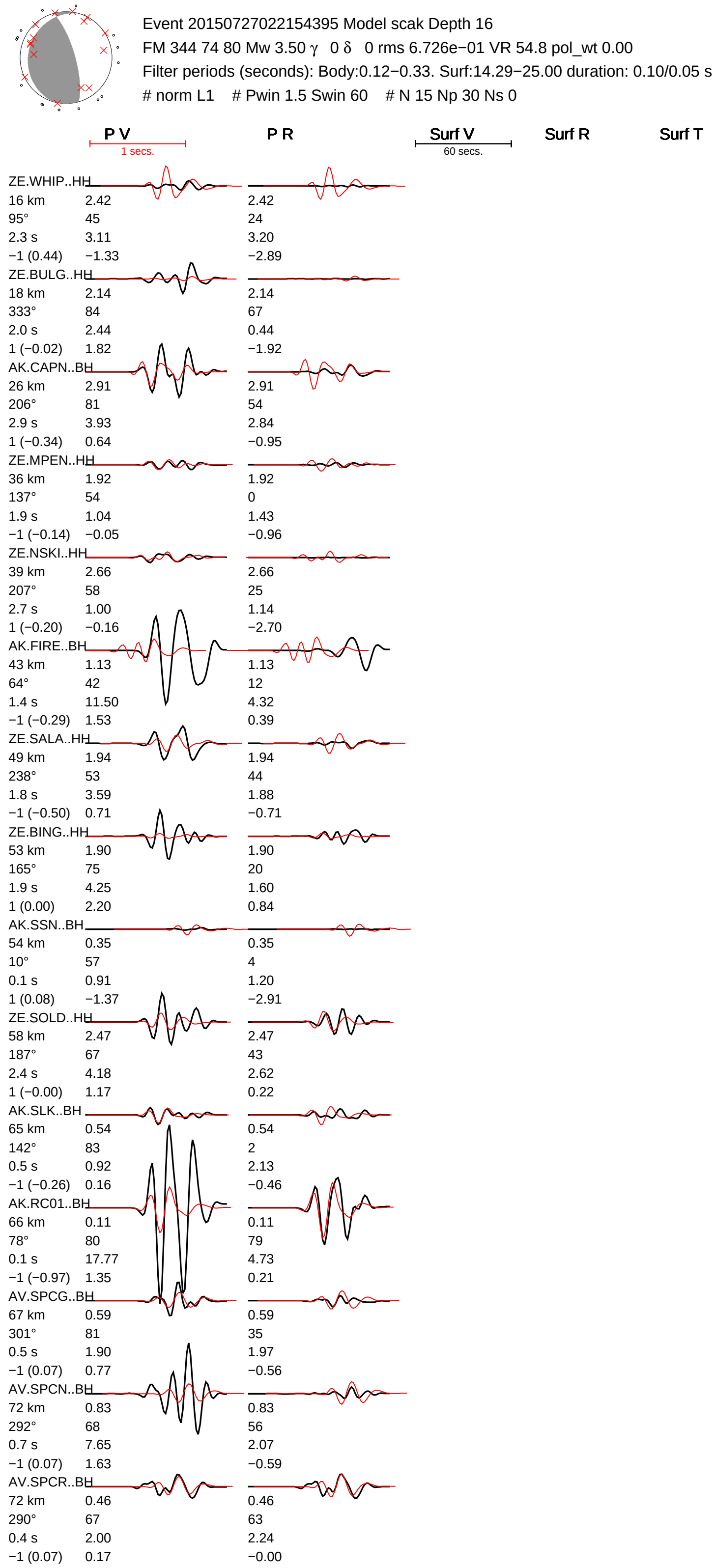

Figure S5: Waveform fits using polarity weight $m = 0.0$. See Figure 10.

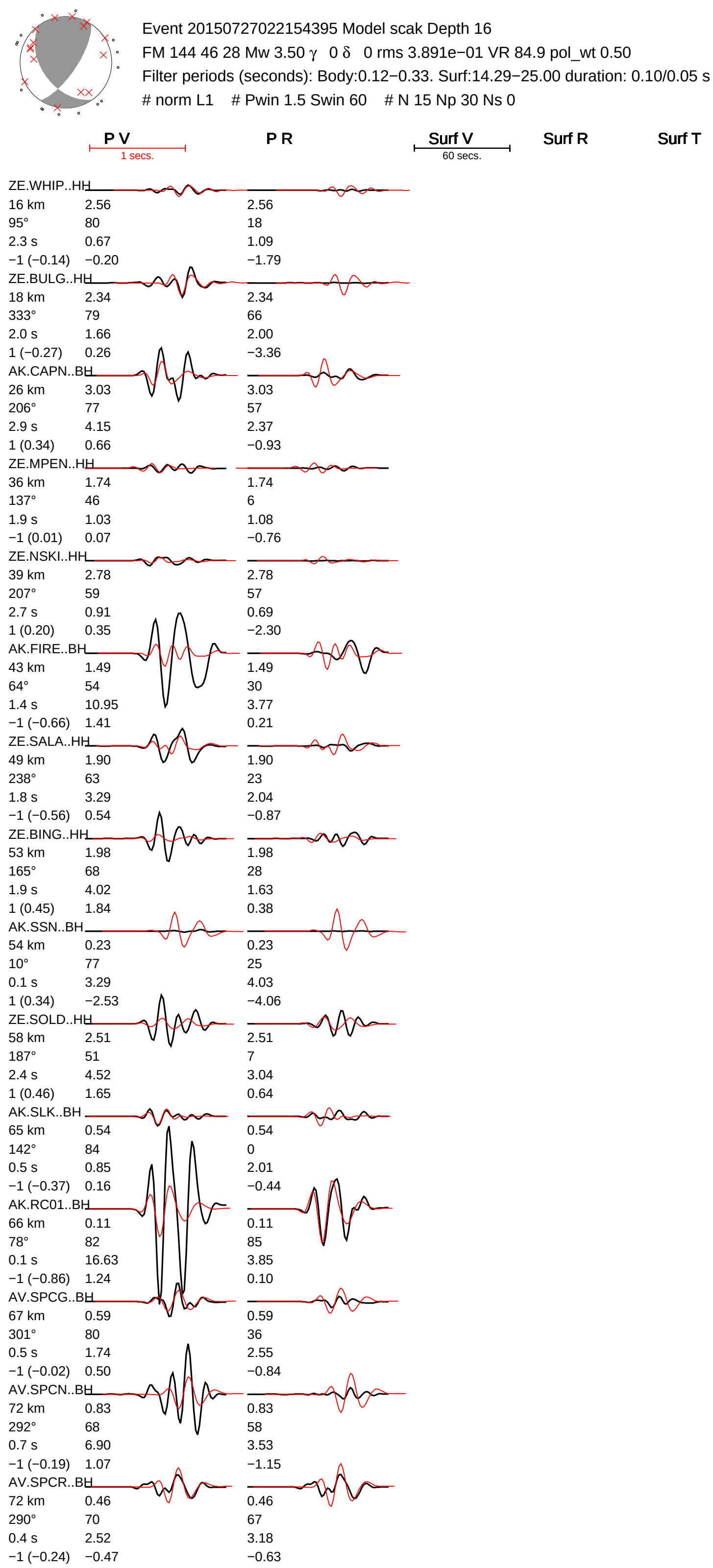

Figure S6: Waveform fits using polarity weight $m = 0.5$. See Figure 10.

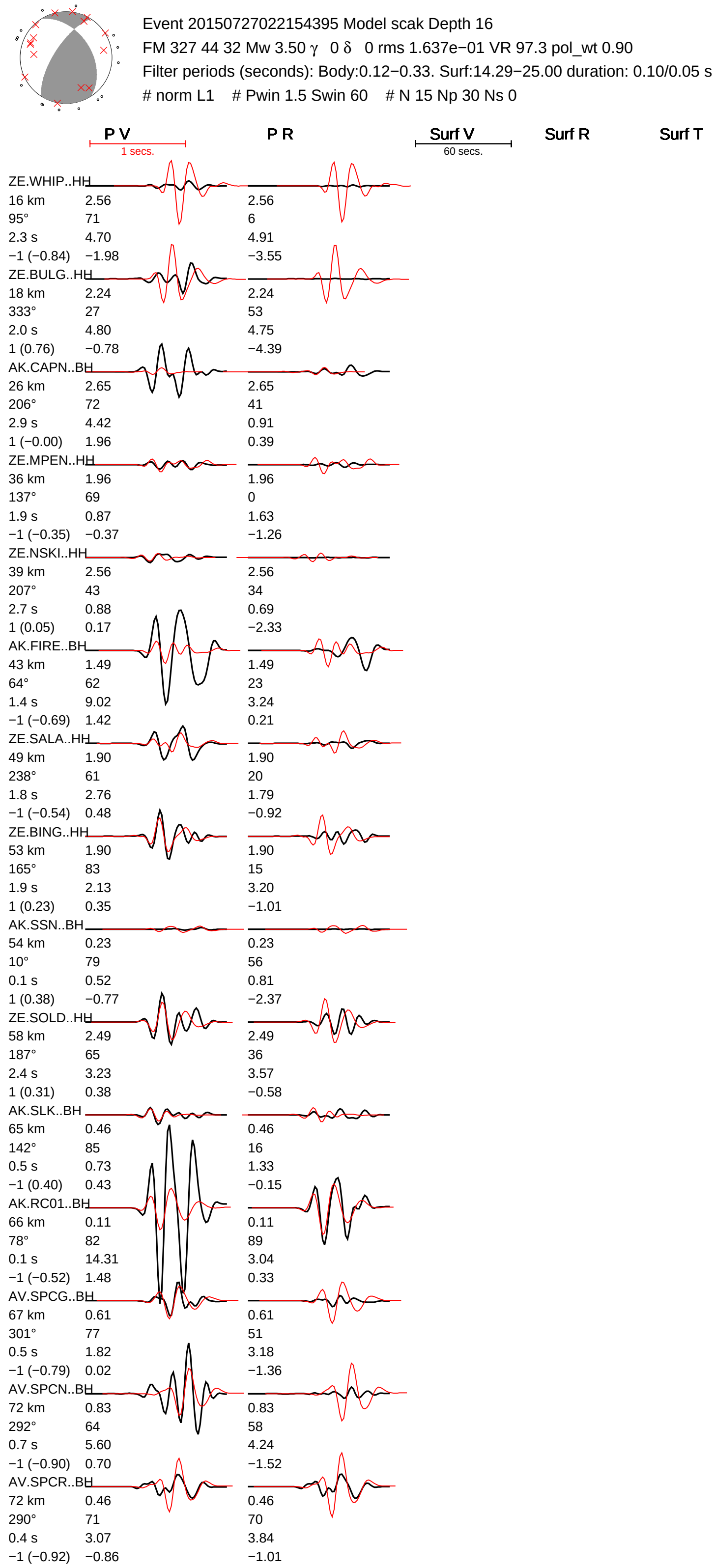

Figure S7: Waveform fits using polarity weight $m = 0.9$. See Figure 10.

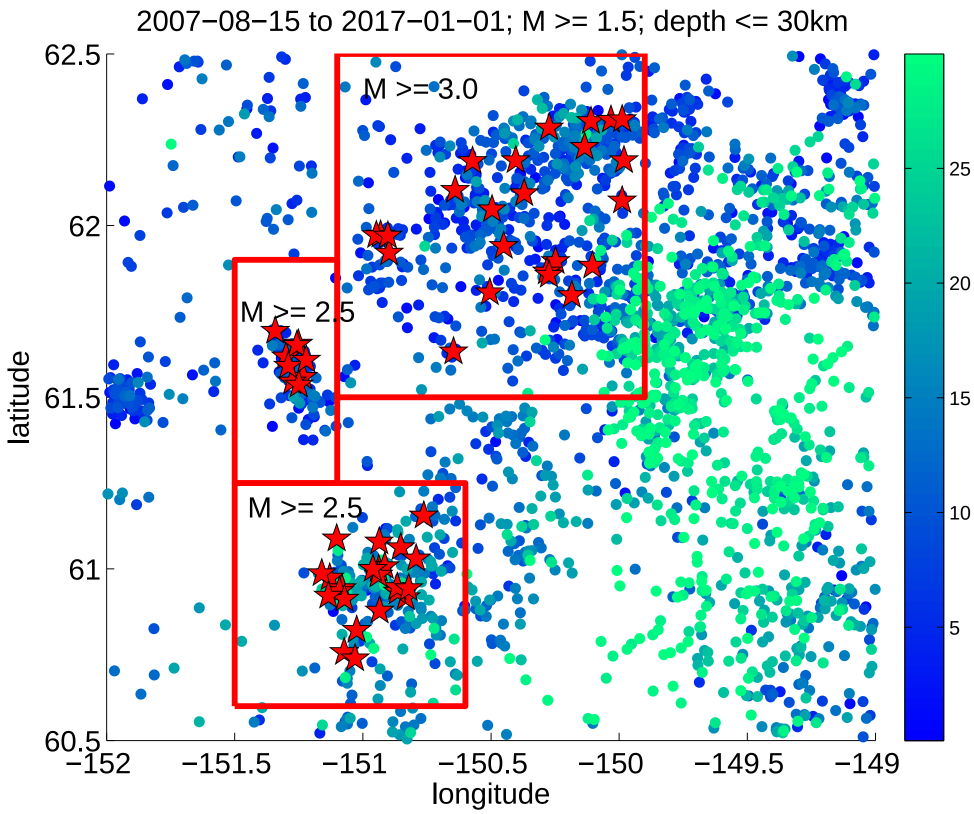

Figure S8: Event selection for moment tensor inversion. AEC catalog with $M_l \geq 1.5$, depth ≤ 30 km, from 2007-08-15 to 2017-01-01. Events are colored by depth, with deeper events (green) plotted on top. Red stars are events that were selected for moment tensor inversion. See Table 1 for region-specific selection criteria.

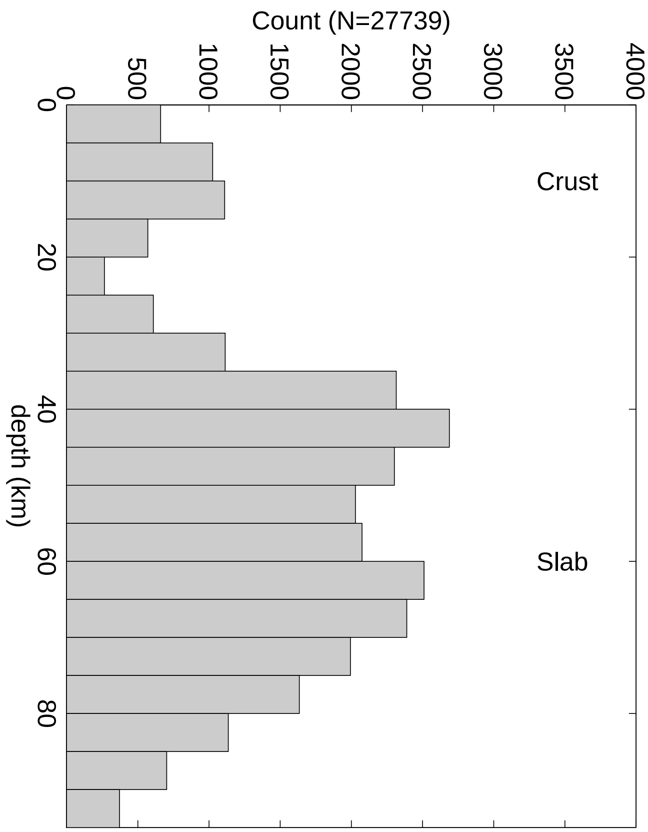

Figure S9: Depth distribution of events $M_l \geq 1.5$ between 1990-01-01 and 2017-01-01 and within the Cook Inlet and Susitna region (Table 1). Above a depth of 30 km, there is a subset of 5726 earthquakes that were used for relocation with hypodd.

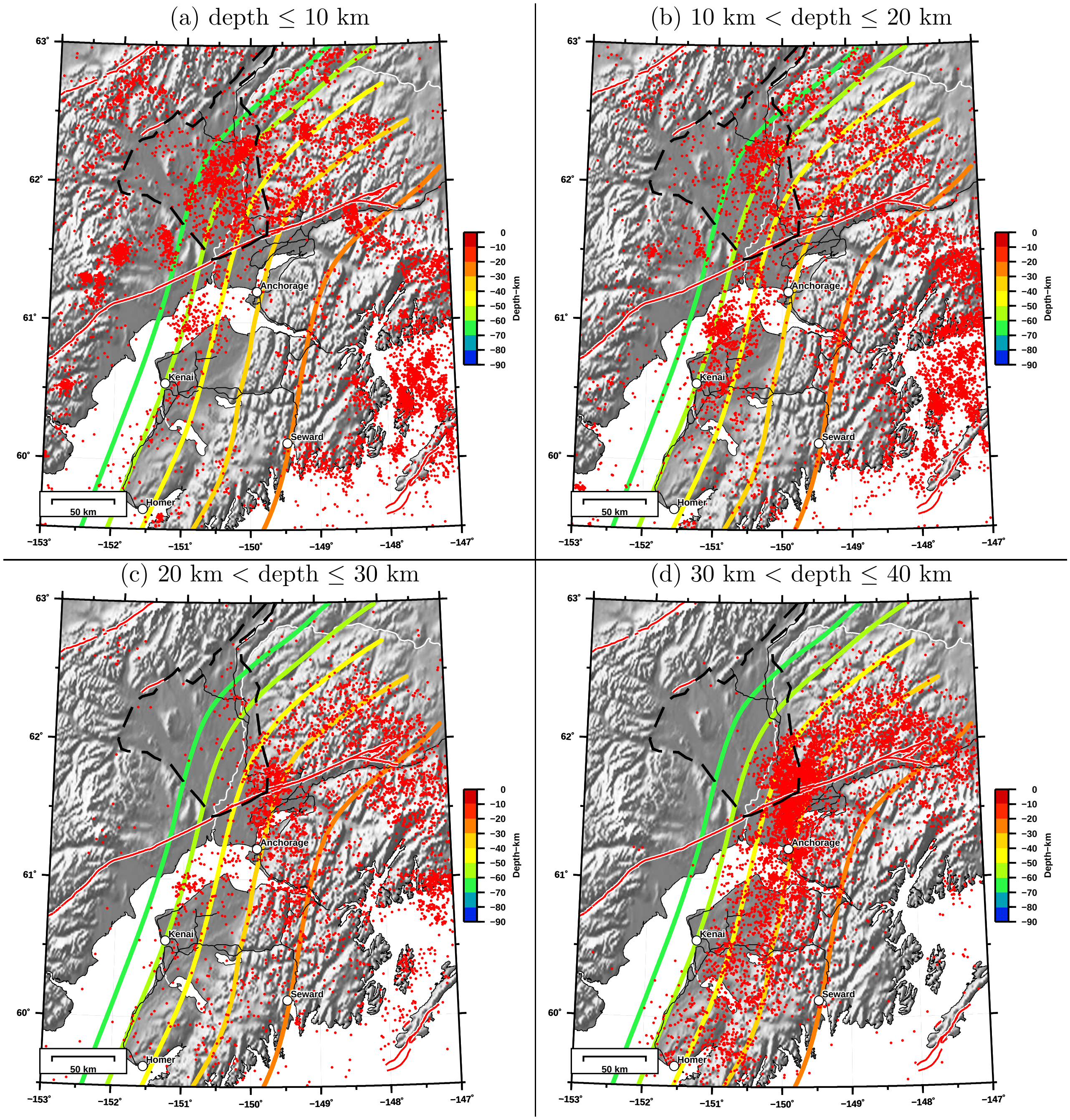

Figure S10: Variation in seismicity with depth for events from 1990-01-01 to 2017-01-01 with magnitude $M_l \geq 1.5$. Earthquakes (in red) are for depth ranges (a) ≤ 10 km, (b) 10–20 km, (c) 20–30 km, and (d) 30–40 km. The colored contours are for the subduction interface (*Li et al.*, 2013) at depths 30, 40, 50, 60, and 70 km. The black dashed line represents the boundary of Susitna basin (*Kirschner*, 1988).

(a) Beluga region

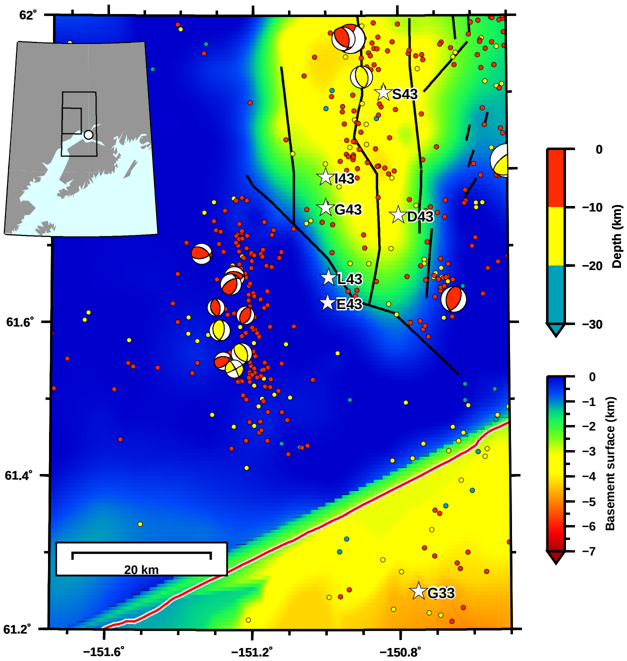

(b) Upper Cook Inlet region

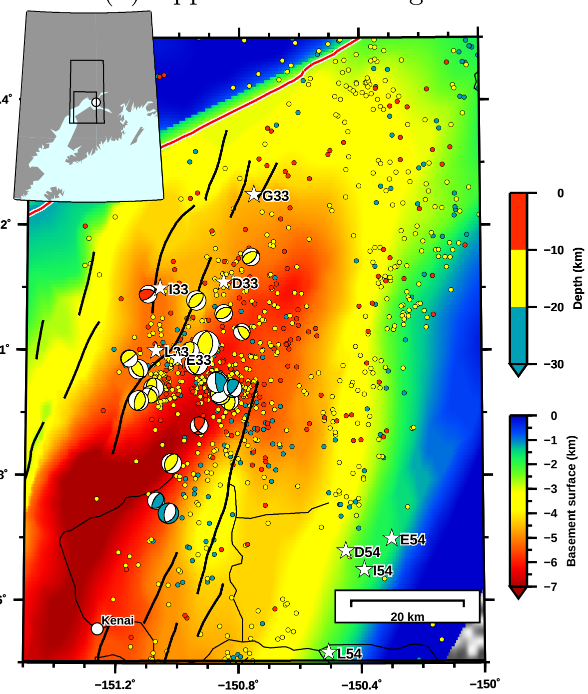

(c) Susitna region

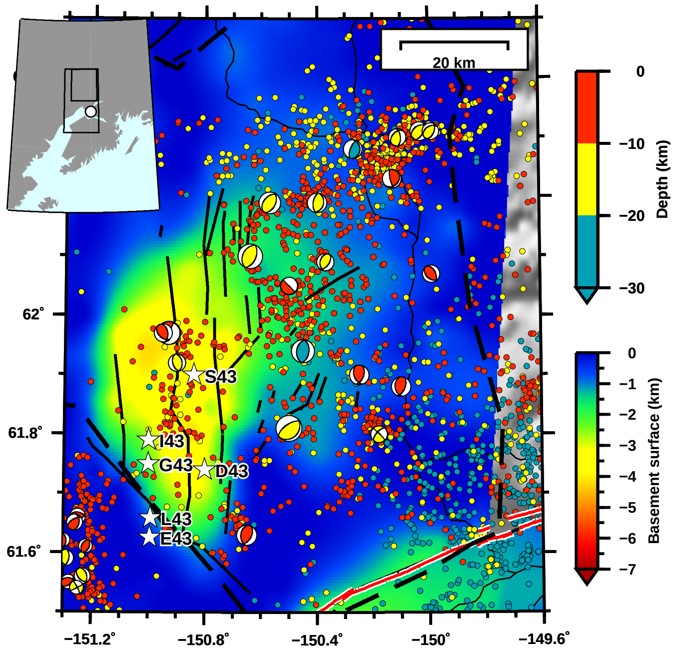

Figure S11: Same as Figure 12, but plotted with an underlying basement surface instead of gray-shaded topography.

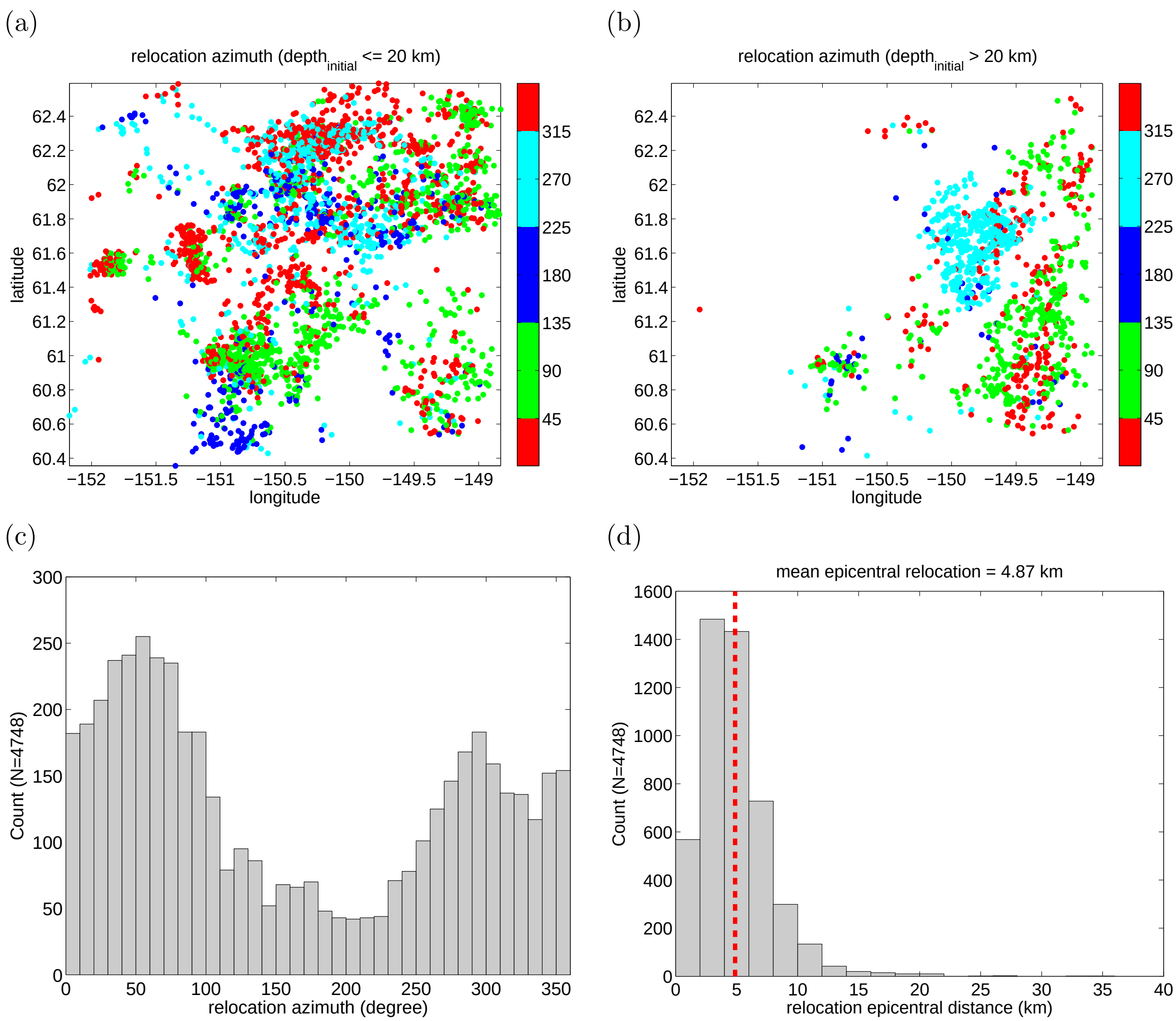

Figure S12: Changes in epicenters due to relocation. (a) Map view representing the azimuth from the initial epicenters to the relocated epicenter for earthquakes ≤ 20 km. Red dots indicate relocations toward the north, dark blue toward the south, cyan toward the west, and green toward the east. (b) Same as (a) but for earthquakes > 20 km. (c) Distribution of the azimuths from the the initial epicenters to the relocated epicenters for all 4748 crustal earthquakes. (d) Distribution of horizontal distances between original and relocated epicenters; the mean difference is 4.87 km.

(a) (b)

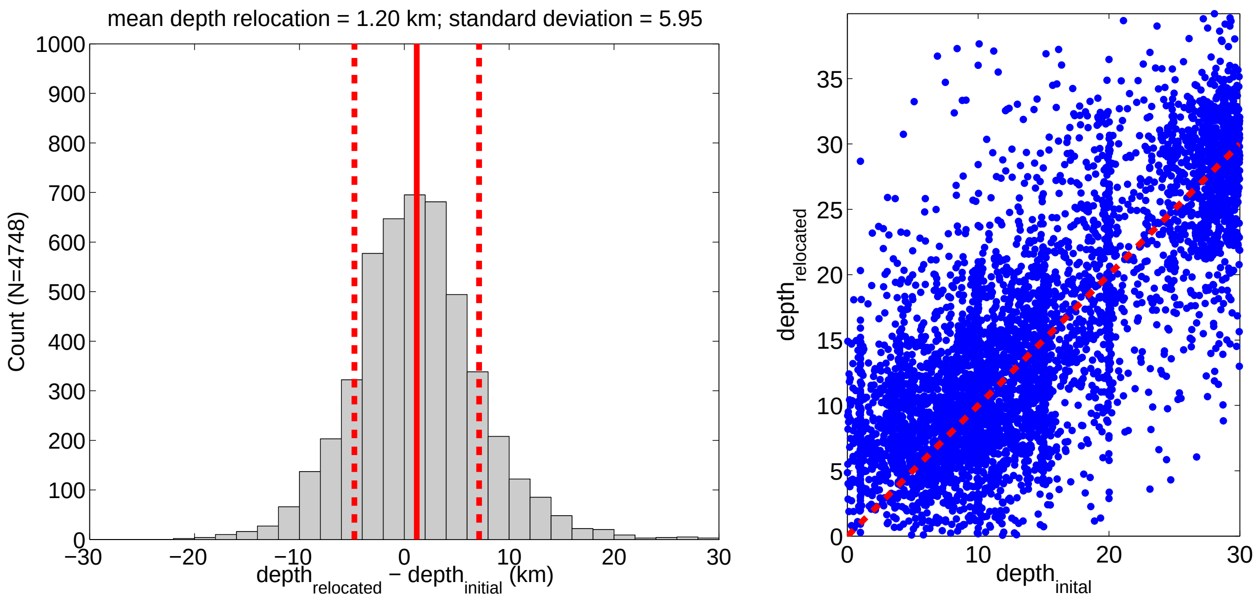

Figure S13: Changes in depths due to relocation. (a) Distribution of changes in depth; the mean and standard deviation are 1.20 km and 5.95 km respectively. (b) Initial depth vs relocated depth. Red dashed line indicates that the relocated depth is same as the final depth. Points above the red dashed line represent events that are relocated to a deeper depth, whereas, for points below the line the events are relocated to a shallower depth.

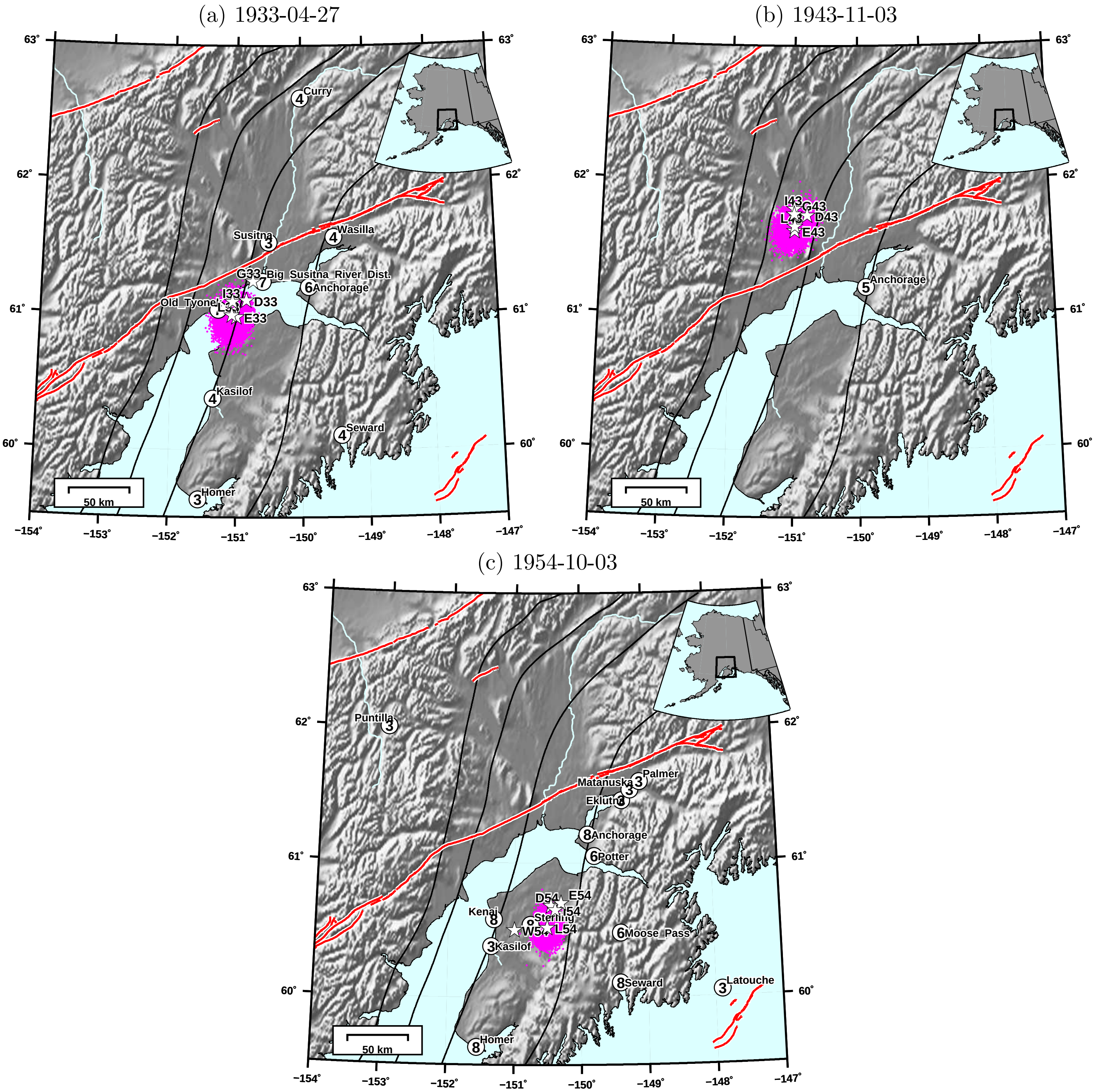

Figure S14: Felt reports from *Brockman et al.* (1988) for the 1933, 1943, and 1954 earthquakes. Note that there are felt reports outside the plotted region for all three earthquakes, and there are felt reports that are not listed in *Brockman et al.* (1988) (e.g., Appendix Appendix A). Also shown for each earthquake is the maximum likelihood epicenter (star) and epicenters of the posterior distribution obtained from NonLinLoc (*Lomax et al.*, 2000). See *Lomax et al.* (2018) for results from other events in Table 2.